

Recirculation regions in wakes with base bleed

K. Steiros¹†, N. Bempedelis² and L. Ding³

¹Department of Aeronautics, Imperial College London, London SW7 2AZ, UK

²Department of Mechanical Engineering, University College London, London WC1E 7JE, UK

³Department of Mechanical and Aerospace Engineering, Princeton University, Princeton, NJ 08544, USA

(Received xx; revised xx; accepted xx)

The appearance of detached recirculation regions in wakes with base bleed determines the aerodynamic properties of many natural organisms and technological applications. Despite that, it remains a controversial phenomenon. In this work we develop a theoretical framework which explains and interprets a half-century of observations. More specifically we explain why the recirculation region (i) emerges, (ii) migrates away from the body with increasing base bleed, (iii) disappears at a critical bleed and (iv) is partially insensitive to variations in the Reynolds number. Our arguments are used to create a predictive model for the wake of porous plates which captures faithfully the basic dimensions of the recirculation region, along with the porosity range that it exists. The predictions show considerable agreement with data from laboratory experiments and numerical simulations.

Key words:

1. Introduction

It is well known that the near wake of bluff bodies is characterized by an attached recirculation region, which determines much of the aerodynamic properties of the configuration (Roshko 1993). An interesting phenomenon occurs when fluid bleeding is superimposed on the wake, i.e. when the body is permeable, or when fluid is actively injected at its base; the recirculation region detaches, and, as fluid bleeding is increased, moves away from the body rear. When bleeding exceeds a critical value, the region suddenly breaks down and disappears.

This behaviour has profound effects on the bluff-body drag and stability of the flow (Castro 1971; Ledda *et al.* 2018). It thus comes as no surprise that several natural organisms have evolved to possess porous membranes (Cummins *et al.* 2018) and wings (Sunada *et al.* 2002), which control the recirculation region and contribute to a more stable and efficient flight. In engineering, base bleed is taken into account when designing efficient airfoils (Bearman 1967; Leal & Acrivos 1969), dynamic mixers (Steiros *et al.* 2017), or when modelling wind turbines and wind farms (Hansen 2008; Ayati *et al.* 2019), to name a few applications.

Despite the above, the reasons behind the emergence, evolution and disappearance of the detached recirculation region remain points of controversy for more than half

† Email address for correspondence: k.steiros13@imperial.ac.uk

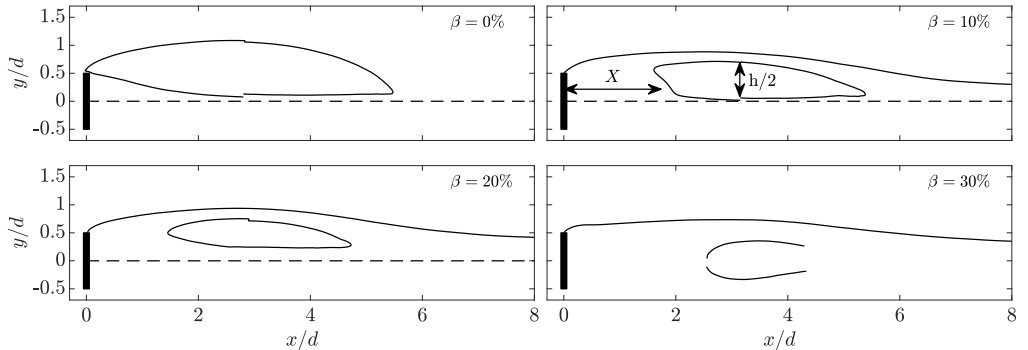


FIGURE 1. Steady wake bubble boundary and slipstream, for different porosity values β , as measured using PIV at $Re = 6 \times 10^3$. X is the bubble detachment length and $h/2$ its half-height. The dashed line signifies the presence of a splitter plate, which was used to stabilize the wake in the cases $\beta = 0, 0.1$ and 0.2 . In the case where $\beta = 0.3$ vortex shedding was suppressed by the large base bleeding (Castro 1971).

a century. In a recent work, Ledda *et al.* (2018) argued that the recirculation region appears as a result of the intense vorticity of the shear layers which induce (according to the Biot-Savart law) back flow velocities in the wake. We note that while the Biot-Savart law is indeed well suited to describe viscous flows (see for instance Wu (1981)), the vorticity magnitude alone is insufficient to act as a causal explanation for the state the flow system settles on. As a matter of fact, several potential flow bluff-body models can be found in the literature (the classical model of Kirchhoff (1869) being one example) which predict large values of shear layer vorticity, but do not include a recirculation bubble in their predictions. Therefore, apart from the magnitude of vorticity, an explanation of the recirculation region must include at least some information on the distribution of this vorticity, which in turn can be thought to be a function of the diffusion process of the flow (turbulent or molecular) and various constraints (e.g. momentum and mass conservation). This fact was not overlooked in the early investigations of Bearman (1967) and Leal & Acrivos (1969) who postulated that the recirculation region is in fact a product of the entrainment process of the free shear layers.

In this paper, we settle the above controversy through a combination of theory, experiments and numerical simulations. We consider the simplest wake with base bleed, that of an infinite-aspect-ratio porous plate, and create a theoretical model which, despite its simplicity, is able to accurately determine the basic dimensions and trends of the bubble. The analysis considers porous plates, but our arguments can be easily extended to the more complex configurations that appear in nature and engineering.

2. Background and preliminary considerations

Figure 1 shows the recirculation bubble of four plates of different porosities at a fully turbulent regime ($Re = 6 \times 10^3$ based on the plate height d and free-stream velocity U_∞), measured using Particle Image Velocimetry (PIV) (the details of the experimental set-up are provided in appendix A.1). The depicted flow fields correspond to “steady” wakes, where vortex shedding is suppressed, either with the use of a splitter plate (cases $\beta = 0, 0.1, 0.2$, where β is the open area ratio defined as the porous plate area over the gross plate area), or from the large base bleeding (case $\beta = 0.3$), which acts as an effective splitter plate (Castro 1971). We note that for the case $\beta = 0.3$ the bubble streamlines did not reconverge to a stagnation point, and for this reason we chose to depict the bubble

as open. We also note that regardless the stabilization technique (splitter plate or wake bleeding), the shear layers will eventually become unstable if allowed to interact, and will generate vortex packets. However, these will be much weaker and will be formed far downstream of the body, compared to the the case where no stabilization is used, so that their effect in the near wake can be thought to be negligible (see discussion in Steiros *et al.* (2020)).

Similar to past investigations (Castro 1971), it is observed that as base bleeding increases, the recirculation bubble detaches from the plate and migrates away from the body, shrinking in size, until it abruptly disappears at a critical open area ratio between $\beta = 0.3$ and $\beta = 0.4$ (no recirculation bubble was observed at $\beta = 0.4$). An analogous behaviour is observed in the laminar regime (Leal & Acrivos 1969), with the difference that the detachment length X increases linearly with Re , whereas in turbulent conditions the bubble dimensions are generally thought to be Re -independent. The bubble height h on the other hand is Re -independent even in the laminar regime (Leal & Acrivos 1969).

Our aim is to explain the above observations, and create a model which can capture, qualitatively, the dimensions X and h , and the porosity range where the bubble exists. Our starting point is the porous plate model of Steiros & Hultmark (2018), which is based on potential flow theory, “corrected” using the constraints of mass and momentum conservation. This model does not predict neither presupposes a recirculation bubble and shear stresses in the wake. Despite that, it yields accurate predictions of the plate drag for any porosity (as long as vortex shedding is absent or suppressed) and wake pressure, p_w , at least for the case where $\beta = 0$. Moreover, the external flow velocities (i.e. outside the wake) have been shown (Graham 1976) to be described reasonably well by the potential flow description that Steiros & Hultmark (2018) use, which is identical to the one presented in Taylor (1944) when considering the outer flow.

Given the above, we perform the assumption that inclusion of the recirculation bubble and shear stresses in the analysis will only alter the wake velocities, and will not affect the plate drag, wake pressure, and wake geometry that are predicted by the modified potential flow model of Steiros & Hultmark (2018). The prediction of Steiros & Hultmark (2018) for the wake velocity after the initial wake expansion, U_w (see figure 2), is given below as it is used repeatedly in the analysis that follows:

$$\frac{U_w}{U_\infty} = \frac{u^*}{2 - u^*}, \quad (2.1)$$

where $u^* = u/U_\infty$ is the plate bypass ratio (see figure 2 for a definition of the flow quantities). This variable is central to the model of Steiros & Hultmark (2018), and is the independent variable of the models developed in the present study. However, in most cases, this is not a readily available quantity. A more straightforward approach would be to express all quantities as a function of the open area ratio β . When the wake is steady and the friction losses through the plate are negligible, β can be approximated by equation (2.2), following the arguments of Taylor & Davies (1944) and Steiros & Hultmark (2018) (see appendix B for the derivation of the equation)

$$\beta \approx \frac{\sqrt{3(u^* - 2)u^*}}{\sqrt{3u^{*3} - 2u^{*2} + 4u^* - 8}}. \quad (2.2)$$

Note that friction losses can be thought to be negligible when the flow is fully turbulent, or when the plate is vanishingly thin. In the remainder of the text, the above equation will be used to express the predictions as a function of β instead of u^* .

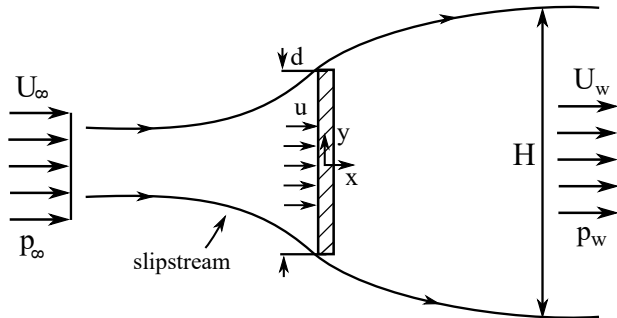


FIGURE 2. Potential flow representation of the steady wake by Steiros & Hultmark (2018). U_∞ and p_∞ denote the free-stream velocity and ambient pressure respectively. U_w and p_w denote the wake velocity and pressure after the initial expansion. H is the wake height after the initial expansion, and d is the plate height. u is the velocity immediately upstream/downstream of the plate.

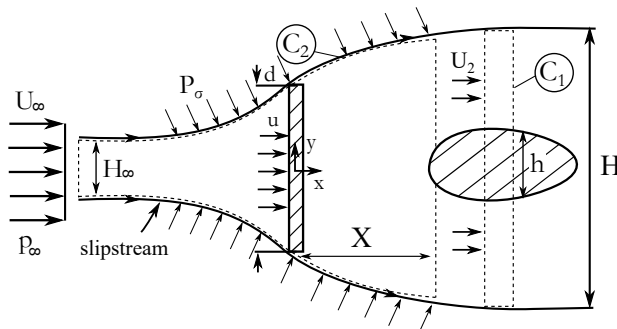


FIGURE 3. Extension of the potential flow representation of the wake of figure 2, by addition of a recirculation region. The dashed regions C_1 and C_2 denote control volumes.

3. Characteristics of the recirculation bubble

3.1. Bubble height and disappearance

We assume the flow field shown in figure 3, where a recirculation bubble is superimposed on the potential flow model depicted in figure 2. The proposed flow model can be realistic only if it is consistent with conservation of mass and momentum. We thus require that these constraints be fulfilled in control volume C_1 , which is positioned at a location where the bubble is sufficiently parallel to the slipstream, so that the characteristic (or y -averaged) flow velocity U_2 between the bubble and the slipstream can be assumed to be approximately constant with the streamwise distance x .

For sufficiently high values of Re , the shear stress on the slipstream or the bubble streamlines is mainly the Reynolds stress $\rho u'v'$. Following Roshko (1993), this can be modelled as $C_t \rho (U_a - U_b)^2$, where U_a and U_b are the velocities at the two sides of the shear layer, and C_t is an empirical coefficient which is assumed to be constant at a first approximation. Application of momentum conservation on control volume C_1 and on the bubble yields

$$\begin{aligned} 2C_t\rho(U_\infty - U_2)^2\delta X &= \delta PH, \\ 2C_t\rho U_2^2\delta X &= \delta Ph, \end{aligned} \quad (3.1)$$

where it was assumed that the velocity outside the wake is U_∞ , and zero inside the bubble. δX is the length of control volume C_1 , and δP is the pressure increase inside the control volume. The factor two is due to the contribution of both (upper and lower) shear layers.

If the bubble were not present, the streamwise velocity at C_1 would be predicted from the potential flow model of Steiros & Hultmark (2018) to be U_w , i.e. the velocity of the expanded wake (given by equation (2.1)). Mass conservation then yields the auxiliary condition

$$\rho U_2(H - h) = \rho U_w H. \quad (3.2)$$

Combination of equations (2.1), (3.1) and (3.2) yields

$$\frac{h}{H} = \left(\frac{u^*}{\left(1 - \frac{h}{H}\right)(2 - u^*) - u^*} \right)^2, \quad (3.3)$$

which links the non-dimensional bubble height h/H with the bypass ratio u^* or, equivalently, with the open area ratio β . The only physically relevant solution to the above equation is

$$\frac{h}{H} = \frac{3u^* - 2 - \sqrt{(u^* - 2)(5u^* - 2)}}{2(u^* - 2)}. \quad (3.4)$$

The predictions of equation (3.4) are plotted in figure 4(a), together with values measured from the PIV experiments and Large-Eddy Simulations (see appendix A for details). The observations are in qualitative agreement with the theoretical predictions. When $u^* > 0.4$, equation (3.4) does not yield real values: the bubble is incompatible with the constraints imposed by momentum and mass conservation. More specifically, the system (3.1) shows that the external shear generates a pressure gradient in the wake, and thus constrains the bubble shear, as the latter must also produce the same pressure gradient. The above can only occur when the bubble has a specific height as this affects on one hand the shear (by changing the velocity between the slipstream and the bubble U_2) and on the other the pressure force on the bubble. Above a critical porosity value no bubble is compatible with the above constraints, and it must therefore disappear. Our simplified model predicts this disappearance to occur at $\beta \approx 0.34$ (which is equivalent to $u^* = 0.4$, according to expression (2.2)). In agreement with that prediction, our measurements indicate that the ‘‘critical’’ porosity β lies somewhere between 0.3 and 0.4, while our simulations predict a critical porosity of $\beta = 0.35$, where the recirculation bubble appears intermittently in time, and is absent when considering the time-averaged flow field.

It must be mentioned that when $\beta \rightarrow 0$ (and $h \rightarrow H$), there is not enough separation between the bubble boundary and the slipstream to consider them as two separate shear layers (see figure 3). In that case, the system of equations (3.1), and thus the above analysis, is not valid. However, equation (3.4) yields the correct prediction of $h/H = 1$ for $\beta = 0$, while we expect the region of invalidity to be small, as for $\beta = 0.1$ the separation of the bubble and slipstream is already of significant extent (see figure 1). We thus use equation (3.4) even when $\beta \rightarrow 0$, and we expect that the deviation from the

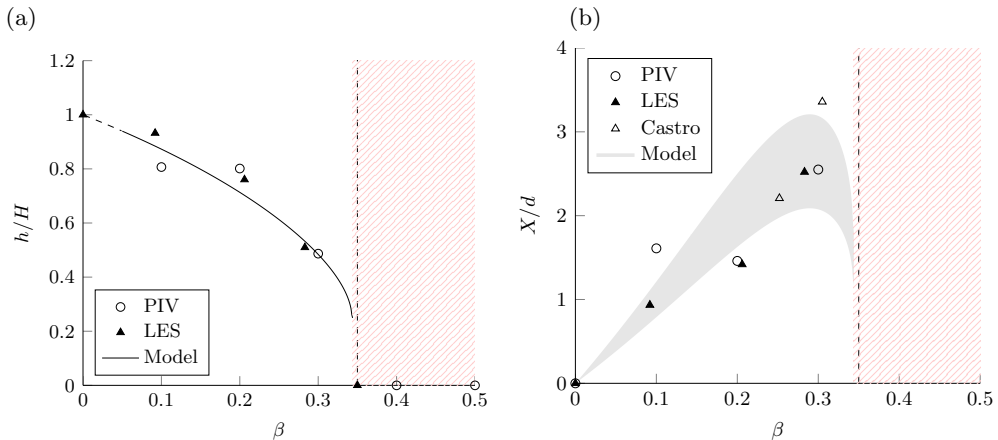


FIGURE 4. Normalized (a) bubble height and (b) detachment length, as a function of β . The dashed part of the prediction marks the region $\beta \rightarrow 0$ where the theoretical analysis is not strictly valid. The hatched areas represent the region where the mass and momentum conservation laws cannot be fulfilled. The dashed vertical line indicates the porosity where the recirculation bubble disappears, according to the numerical simulations. Where available, results from the experiments of Castro (1971) are also included.

“correct” prediction is small. To emphasize the above, the part of the prediction where we expect it to not be strictly valid has been marked with a dashed line in figure 4(a).

3.2. Bubble detachment and emergence

We now consider control volume C_2 (see figure 3), which is bounded by the slipstream, and extends from far upstream of the plate to the tip of the bubble, i.e. at distance X from the plate. As argued in section 2, we assume that the pressure at this location is equal to p_w , i.e. the wake pressure as predicted by Steiros & Hultmark (2018). If the bubble and shear stresses were absent from the analysis, the problem would be reduced to the one of Steiros & Hultmark (2018), and in that case, a momentum balance in C_2 would yield

$$D = \rho u d(U_\infty - U_w) + p_\infty H_\infty - p_w H + P_\sigma, \quad (3.5)$$

where D is the drag and P_σ is the pressure force on the slipstream. Steiros & Hultmark (2018) employed a slightly different control volume, but under identical assumptions, and their results are thus equivalent.

We now increase the complexity of the analysis by adding a bubble and shear stress on the slipstream. As argued in section 2, it is assumed that only the wake velocities are altered from the added complexity. Thus, a momentum balance in C_2 now yields

$$D = \rho u d(U_\infty - U_2) + p_\infty H_\infty - p_w H + P_\sigma + F_s. \quad (3.6)$$

For high Re , the forcing on the slipstream F_s is mainly the Reynolds stress. Similar to the discussion in section 3.1, this is modelled as being proportional to the square of the velocity difference across the slipstream. A reasonable approximation is to consider the outside velocity to be U_∞ , and the inside one to be u . Thus, the force due to shear stress becomes

$$F_s \approx 2\rho C_t (U_\infty - u)^2 X, \quad (3.7)$$

where the factor 2 is due to the two (upper and lower) shear layers, and C_t a constant (provided from experiments or numerical simulations). Combining equations (3.5), (3.6) and (3.7) we obtain

$$2\rho C_t(U_\infty - u)^2 X \approx \rho u d(U_2 - U_w). \quad (3.8)$$

We interpret the above equation by following an analogous argument as Bearman (1967) and Leal & Acrivos (1969): immediately downstream of the plate, the shear on the slipstream will cause an acceleration of the wake fluid which is closest to the slipstream and, in order for mass to be conserved, the fluid at the core of the wake will have to be continually decelerated. When it reaches zero velocity, a recirculation bubble will form. At this exact location, the momentum flux will be approximately $\rho u d U_2$, i.e. increased by $\rho u d(U_2 - U_w)$ compared with the case where a bubble is not included in the flow description. Our simplified analysis assumes that this increase in momentum flux is exactly provided by the shear stress on the slipstream.

Combination of equations (2.1), (3.2), (3.4) and (3.8), leads to the following expression for the normalized detachment length X/d

$$\frac{X}{d} = \frac{1}{2C_t} \frac{u^{*2}}{(1-u^*)^2(2-u^*)} \frac{3u^* - 2 - \sqrt{(u^* - 2)(5u^* - 2)}}{\sqrt{(u^* - 2)(5u^* - 2)} - u^* - 2}, \quad (3.9)$$

where C_t must be determined from the shear stress on the part of the slipstream which extends from the plate to the start of the bubble. As described in appendix A, by integrating the shear stresses on the slipstream up until the bubble, and then averaging across all tested cases, we obtain a value of $C_t = 0.0257$ for our laboratory, and $C_t = 0.0395$ for our numerical experiments. These values are somewhat different, but we note that our region of integration lies very close to the plate, and is thus extremely inhomogeneous and sensitive to boundary conditions (which differ between the simulations and experiments).

In figure 4(b) we plot equation (3.9) using the above two values of C_t to form an envelope. We observe that the predictions are in qualitative agreement with the predicted/measured values of X/d , suggesting that our theoretical arguments are not far from what occurs in reality.

3.3. Laminar regime

The analysis presented in the above sections concerns the fully turbulent regime, where the bubble dimensions are expected to be independent of the Reynolds number, in accordance with equations (3.4) and (3.9). In the laminar regime on the other hand, Leal & Acrivos (1969) observed that while the normalized height of the bubble remains *Re*-independent, the detachment length X increases linearly with *Re*. We will now explain these observations using the proposed framework.

We consider a steady laminar wake and assume that the present analysis is capable of describing the flow field. At first this seems counter-intuitive, given that one would expect that an analysis based on potential flow theory is likely to be valid only for very high, close to infinite, Reynolds numbers. Nevertheless, the results of Acrivos *et al.* (1965) and Leal & Acrivos (1969) indicate that an “infinite” *Re* analysis may be appropriate for bluff bodies whose Reynolds numbers are as low as 25.

The analysis presented in sections 3.1 and 3.2 may thus be repeated, with the only difference being that the stresses on the slipstream and bubble are now predominantly

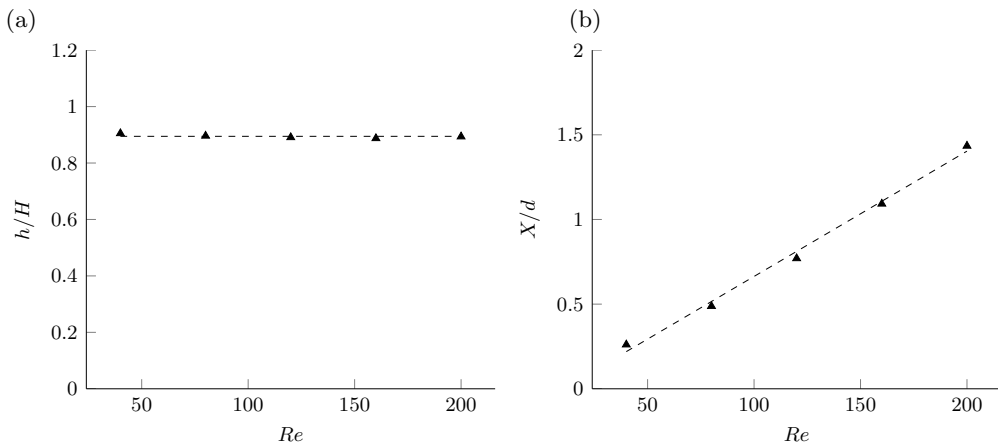


FIGURE 5. Normalized (a) bubble height and (b) detachment length, as a function of Re in the laminar regime, for a thin plate where $\beta = 20.6\%$. Symbols: DNS. Line: linear fit.

viscous rather than turbulent. These are modelled using a standard boundary layer analysis with l as the characteristic length:

$$F_s = C_v \mu \frac{U_a - U_b}{l} \sqrt{Re_l}, \quad (3.10)$$

where μ is the dynamic viscosity of the fluid, $(U_a - U_b)$ is the velocity difference across the shear layer and C_v is a coefficient of proportionality. A momentum budget similar to the one presented in section 3.1 now yields the following system of equations

$$\begin{aligned} 2C_v \mu \frac{U_\infty - U_2}{l_1 Re_{l_1}^{-1/2}} \delta X &= \delta P H, \\ 2C_v \mu \frac{U_2}{l_2 Re_{l_2}^{-1/2}} \delta X &= \delta P h. \end{aligned} \quad (3.11)$$

Calculation of the normalized bubble height h/H requires taking the ratio of the above equations, and thus any dependency on viscosity cancels out, as per the observations of Leal & Acrivos (1969).

With respect to the detachment length, the laminar equivalent of equation (3.8) is

$$2C_v \nu (U_\infty - u) \sqrt{\frac{U_\infty X}{\nu}} = u d (U_2 - U_w), \quad (3.12)$$

where $\nu = \mu/\rho$. This can be rearranged to yield

$$\frac{X}{d} = Ref(u^*), \quad (3.13)$$

which predicts a linear increase of the detachment length with Re in the laminar regime, as per the observations of Leal & Acrivos (1969).

In figure 5 we examine the validity of the predicted trends by comparing them with data from a series of Direct Numerical Simulations (DNS) of a thin plate of $\beta = 20.6\%$, for $40 \leq Re \leq 200$ (see appendix A for numerical details). In accordance with our theoretical predictions, the bubble height is independent of the Reynolds number, while the detachment length grows linearly with Re .

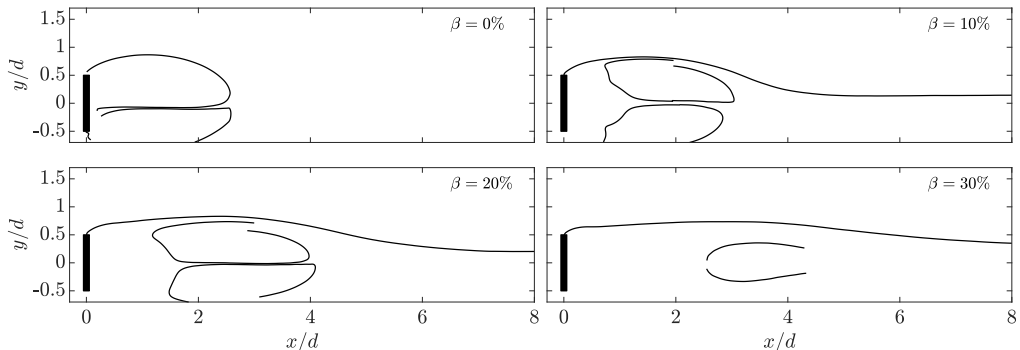


FIGURE 6. Time-averaged recirculation bubble for different values of porosity β , as measured using PIV, at $Re = 6 \times 10^3$. Vortex shedding makes the wake unsteady for $\beta = 0, 0.1$ and 0.2 , but is suppressed for $\beta = 0.3$ due to the large bleeding (Castro 1971). The bubble evolution is qualitatively similar to the case where the wake is stabilized using a splitter plate (figure 1).

3.4. Extensions

The above models concern the recirculation region that appears in the steady wake of porous plates, given that the basis of our analysis is the potential flow model of Steiros & Hultmark (2018). Nevertheless, the physical arguments that are presented in this study, along with the various explanations and interpretations, are general, and apply to the detached recirculation regions that characterize many other wakes with base bleed that appear in nature and engineering.

A pertinent example is those wakes in which bleeding is generated by actively injecting fluid in the wake, rather than passively perforating the body. Such apparatuses are relevant, for instance, to bluff airfoil flow control (Bearman 1967; Leal & Acrivos 1969). In such cases, a recirculation bubble again appears, which shares all the characteristics and trends of the recirculation bubble of porous plates, albeit possessing different characteristic dimensions. Another example is the wake of various flowers and seeds. Despite their complexity, these organisms generate wakes and detached recirculation regions which are remarkably similar to those of porous plates (Cummins *et al.* 2018).

When the wake becomes unsteady due to the emergence of vortex shedding, a similar recirculation bubble appears in the time-averaged field; its trends and physics are qualitatively similar to the steady case (see figure 6). The arguments of the present study are then applicable, in a qualitative sense, even though the actual wake dimensions cannot be accurately described by the theory presented here, which concerns steady wakes.

Appendix A. Details of experimental and numerical methods

A.1. Experimental apparatus and data processing

The validation experiments were conducted in a free-surface recirculating water tunnel. The tunnel had a 0.46 m wide, 0.3 m deep and 2.44 m long acrylic test section, and operated at a constant free-stream velocity of 0.2 ms^{-1} . The experimental set-up is shown in figure 7.

Porous plates with porosities $\beta = 0\%$ (solid), 10%, 20%, \dots , 60% porosity were tested. The plates were 29 cm high, 3 cm wide and 0.3 cm thick, and were perforated with circular holes arranged in the way depicted in figure 7. The hole diameter was varied to achieve different porosities. In the experiments, the plates were supported from the top and were positioned near the center of the test section. The plates touched the floor of the channel

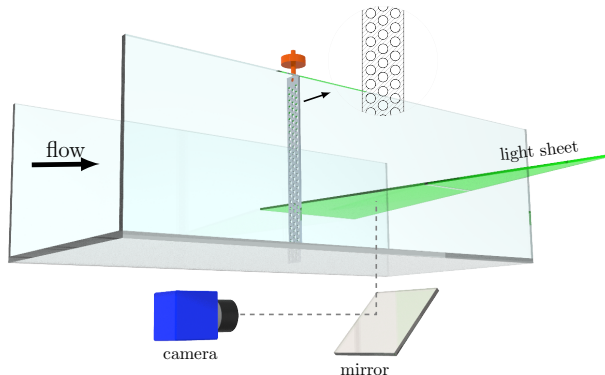


FIGURE 7. Experimental set-up for PIV measurements.

at one end, while the other end extended above the water free surface, in order to suppress three-dimensional effects arising from the plate edges. For porosities 0%, 10% and 20%, a long splitter plate (~ 10 plate widths) was positioned at the wake of the plate, in order to stabilize the wake by suppressing the vortex shedding which otherwise appears at these porosities (Castro 1971).

Planar PIV was performed to study the evolution of the recirculation bubble. A dual-cavity Nd:YAG laser (Litron Nano PIV, 50 mJ pulses) was used to form a light sheet at half depth of the tunnel. A PIV camera (LaVision Imager sCMOS) was situated underneath the tunnel to image the wake through the reflection of a mirror. A $2\times$ teleconverter (Vivitar) was attached to the camera yielding a magnification of 0.16. In the cross-stream direction, the field of view covered the full width of the plate plus another 2.3 plate widths on a single side of the plate. In the streamwise direction, velocity data were acquired at five stations that spanned over 12 plate widths downstream of the plate. Different downstream stations were accessed by traversing the plate upstream while keeping the camera and mirror fixed, since the free stream in the middle portion of the test section was homogeneous. A small overlap region between the measurement planes allowed their subsequent stitching, by finding the location where the velocity profiles from two different planes collapsed in an optimal manner.

At each station, 1,000 image pairs were recorded and analyzed to calculate flow statistics. PIV interrogation was performed in DaVis 8.3 using a multi-grid, image deformation strategy (Scarano 2001), with a final interrogation spot size of $2\text{ mm} \times 2\text{ mm}$ and 50% window overlap. Velocity vectors were validated with the universal outlier detection method (Westerweel & Scarano 2005).

The bubble boundary was found by locating the streamlines that reversed their direction in the wake, and then choosing the one that created the largest bubble. It was often the case that two streamlines were stitched together to form the bubble boundary: one for the front change of direction (bubble tip), and one for the rear. The slipstream was found by locating the streamline that passed from the plate edge. The coefficient C_t in the discussion of section 3.2 was found by calculating the normalized turbulent stress $\overline{u'v'}/(U_\infty - u)^2$ on the slipstream, from a location $0.15d$ downstream of the plate, to the location where the bubble emerged, and then taking its average value (u^* was calculated using equation 2.2). The downstream distance $0.15d$ was chosen as a compromise between starting the averaging process as close as possible to the plate, and far enough, in order to minimize the noise due to reflections and shadows. For the cases where a steady bubble emerged, (i.e. $\beta = 0, 0.1$ and 0.2 with splitter plate and $\beta = 0.3$ without splitter plate), C_t

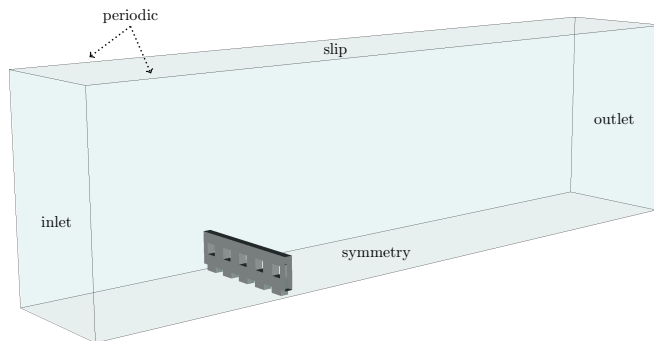


FIGURE 8. Computational set-up for simulations of the flow past porous plates (domain and plate not drawn to scale).

was calculated equal to 0.0257 ± 0.002 . The ratio h/H was calculated at the maximum bubble width, and the distance X as the minimum distance between the bubble and the plate.

A.2. Numerical simulations

Simulations were performed using the general-purpose finite-volume toolbox OpenFOAM. For the turbulent flow cases, where the Reynolds number based on the plate height and free-stream velocity was $Re = 6240$, Large-Eddy Simulations (LES) using the dynamic one-equation subgrid-scale model of Kim & Menon (1995) were performed. For the simulations in the laminar regime (section 3.3), the sub-grid scale model was dropped, and Direct Numerical Simulations (DNS) were conducted. The convective terms were discretized with a second-order central differencing scheme. A second-order backward scheme was used for time discretization.

The porosity of the plates was controlled by changing the size of the homogeneously distributed rectangular-shaped holes. For the simulations in the turbulent regime, the width of the plates was similar to those in the experiment, $\approx 10\%$ of the plate height d . A total of five plates were considered, with porosities equal to $\beta(\%) = 0, 9.2, 20.6, 28.3, 35$. In the laminar flow cases, the plate that was considered was thinner ($\approx 1.77\%$ of the plate height d), so as to minimize viscous effects due to the friction inside the plate holes, which can be significant at low Reynolds numbers.

Communication of the upper and lower layers was inhibited by simulating only half the plate and enforcing symmetry conditions along the centreline. Vortex shedding was therefore suppressed, in a similar way as when a splitter plate is used. The computational domain consisted of a rectangular box extending $27.5 \times 8 \times 1.7$ times the plate height d in the streamwise, normal, and spanwise directions, respectively (see figure 8). Laminar inflow was imposed at the upstream boundary, whereas periodic boundary conditions were applied in the spanwise direction. The spanwise extent of the domain was taken such that precisely five holes could be accommodated. The domain was discretized with $\simeq 3.0 \times 10^6$ elements in the turbulent flow cases, and $\simeq 1.8 \times 10^6$ in the laminar ones. In all cases, 50 cells were used along the span. Data were averaged over a non-dimensional time period corresponding to $t^* = tU_\infty/d = 104$ flow times.

Validation of the numerical simulations was performed against the PIV measurements (section A.1), for the case where $\beta = 30\%$ (the plate porosity in the simulations was $\beta = 28.3\%$). A set-up that better replicated the experiments was considered, with the domain doubled in size in the normal direction, so that the entire plate could be

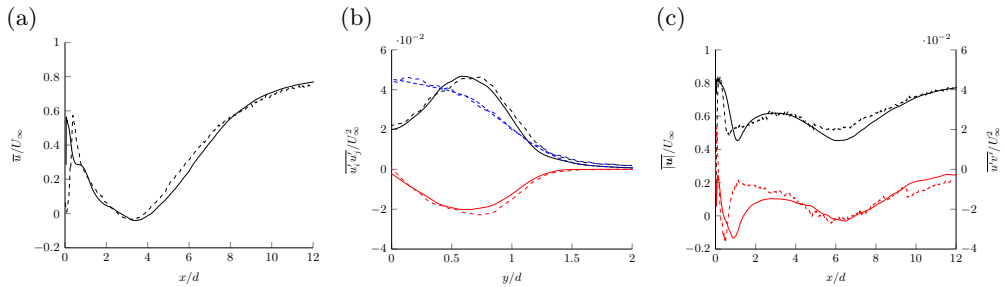


FIGURE 9. (a) Streamwise velocity along wake centreline. (b) Reynolds stresses at a cut in the wake at $x/d = 5$. Black: $\overline{u'v'}/U_\infty^2$, red: $\overline{u'v'}/U_\infty^2$, blue: $\overline{v'v'}/U_\infty^2$. (c) Black: velocity magnitude and red: Reynolds stress ($\overline{u'v'}/U_\infty^2$) along the slipstream. Time-averaged results. Dashed lines: PIV measurements (from a single plane), solid lines: numerical simulations (averaged over the spanwise extent of the domain).

accommodated (i.e. the symmetry condition was removed). This change mostly affected the flow downstream of the bubble, whereas the key dimensions of the bubble that are discussed in the main body of the paper were largely unaffected. The results from the laboratory and numerical experiments are compared in figure 9; good agreement between the two is observed.

Appendix B. Derivation of equation (2.2)

Steiros & Hultmark (2018) provide the following expression for the drag coefficient of an infinite-aspect-ratio plate, for a steady wake and fully turbulent regime:

$$C_D = \frac{4}{3} \frac{(1 - u^*)(2 + u^*)}{2 - u^*}. \quad (\text{B1})$$

On the other hand, Taylor & Davies (1944) show that the plate drag can also be approximated by the following expression when the regime is fully turbulent.

$$C_D \approx u^{*2} \left(\frac{1}{\beta^2} - 1 \right). \quad (\text{B2})$$

The critical assumption of the above equation is that the surplus kinetic energy, due to acceleration, of the fluid which enters the plate pores, becomes irreversibly heat, due to the expansion at the end of the pores. Combination of the above two equations yields equation (2.2).

Declaration of interests

The authors report no conflict of interest.

REFERENCES

- ACRIVOS, A., SNOWDEN, D. D., GROVE, A. S. & PETERSEN, E. E. 1965 The steady separated flow past a circular cylinder at large reynolds numbers. *Journal of Fluid Mechanics* **21** (4), 737–760.
- AYATI, A. A., STEIROS, K., MILLER, M. A., DUVVURI, S. & HULTMARK, M. 2019 A double-multiple streamtube model for vertical axis wind turbines of arbitrary rotor loading. *Wind Energy Science* **4** (4), 653–662.

- BEARMAN, P. W. 1967 The effect of base bleed on the flow behind a two-dimensional model with a blunt trailing edge. *The Aeronautical Quarterly* **18** (3), 207–224.
- CASTRO, I. P. 1971 Wake characteristics of two-dimensional perforated plates normal to an air-stream. *Journal of Fluid Mechanics* **46** (3), 599–609.
- CUMMINS, C., SEALE, M., MACENTE, A., CERTINI, D., MASTROPAOLO, E., VIOLA, I. M. & NAKAYAMA, N. 2018 A separated vortex ring underlies the flight of the dandelion. *Nature* **562** (7727), 414–418.
- GRAHAM, J. M. R. 1976 Turbulent flow past a porous plate. *Journal of Fluid Mechanics* **73** (3), 565–591.
- HANSEN, M. O. L. 2008 *Aerodynamics of wind turbines*. Earthscan.
- KIM, W-W. & MENON, S 1995 A new dynamic one-equation subgrid-scale model for large eddy simulations. In *33rd Aerospace Sciences Meeting and Exhibit*.
- KIRCHHOFF, G. 1869 Zur theorie freier flüssigkeitsstrahlen. *Journal Für die Reine und Angewandte Mathematik* (70), 289–298.
- LEAL, L. G. & ACRIVOS, A. 1969 The effect of base bleed on the steady separated flow past bluff objects. *Journal of Fluid Mechanics* **39** (4), 735–752.
- LEDDA, P. G., SICONOLFI, L., VIOLA, F., GALLAIRE, F. & CAMARRI, S. 2018 Suppression of von Kármán vortex streets past porous rectangular cylinders. *Physical Review Fluids* **3** (10), 103901.
- ROSHKO, A. 1993 Perspectives on bluff body aerodynamics. *Journal of Wind Engineering and Industrial Aerodynamics* **49** (1-3), 79–100.
- SCARANO, F. 2001 Iterative image deformation methods in PIV. *Measurement Science and Technology* **13** (1), R1.
- STEIROS, K., BRUCE, P. J. K., BUXTON, O. R. H. & VASSILICOS, J. C. 2017 Effect of blade modifications on the torque and flow field of radial impellers in stirred tanks. *Physical Review Fluids* **2** (9), 094802.
- STEIROS, K. & HULTMARK, M. 2018 Drag on flat plates of arbitrary porosity. *Journal of Fluid Mechanics* **853**, R3.
- STEIROS, K., KOKMANIAN, K., BEMPEDELIS, N. & HULTMARK, M. 2020 The effect of porosity on the drag of cylinders. *Journal of Fluid Mechanics* **901**, R2.
- SUNADA, S., TAKASHIMA, H., HATTORI, T., YASUDA, K. & KAWACHI, K. 2002 Fluid-dynamic characteristics of a bristled wing. *Journal of Experimental Biology* **205** (17), 2737–2744.
- TAYLOR, G. I. 1944 Air resistance of a flat plate of very porous material. *Aeronautical Research Council, Reports and Memoranda* **2236**.
- TAYLOR, G. I. & DAVIES, R. M. 1944 The aerodynamics of porous sheets. *Aeronautical Research Council, Reports and Memoranda* **2237**.
- WESTERWEEL, J. & SCARANO, F. 2005 Universal outlier detection for PIV data. *Experiments in Fluids* **39** (6), 1096–1100.
- WU, J. C. 1981 Theory for aerodynamic force and moment in viscous flows. *AIAA Journal* **19** (4), 432–441.